# Synthetic Ligand Selection Affects Stoichiometry, Carrier Dynamics, and Trapping in CuInSe<sub>2</sub> Nanocrystals

Samantha M. Harvey<sup>1,2</sup>, Daniel W. Houck<sup>3</sup>, Wen Liu<sup>3</sup>, Yuzi Liu<sup>4</sup>, David J. Gosztola<sup>4</sup>, Brian A. Korgel<sup>3</sup>, Michael R. Wasielewski<sup>1,2</sup>, Richard D. Schaller<sup>1,4</sup>\*

# **Abstract**

CuInSe2 nanocrystals exhibit tunable near-infrared bandgaps that bolster utility in photovoltaic applications as well as offer potential as substitutes for more-toxic Cd- and Pb-based semiconductor compositions. However, they can present a variety of defect states as well as unusual photophysics. Here, we examine the effects of ligand composition (oleylamine, diphenylphosphine, and tributylphosphine) on carrier dynamics in these materials. *Via* spectroscopic measurements such as photoluminescence and transient absorption, we find that ligands present during the synthesis of CuInSe2 nanocrystals impart non-radiative electronic states which compete with radiative recombination and give rise to low photoluminescence quantum yields. We characterize the nature of these defect states (hole *vs.* electron traps) and investigate whether they exist at the surface or interior of the nanocrystals. Carrier lifetimes are highly dependent on ligand identity where oleylamine-capped nanocrystals exhibit rapid trapping (< 20 ps) followed by diphenylphosphine (< 500 ps) and finally tributylphosphine (> 2 ns). A majority of carrier population localizes at indium copper antisites (electrons), copper vacancies (holes), or surface traps (electrons and/or holes), all of which are non-emissive.

**Keywords:** copper indium selenide, semiconductor nanocrystals, defects, carrier dynamics, ligands

Colloidal semiconductor nanocrystals (NCs) garner significant interest owing to their optoelectronic properties that derive from size-dependent quantum confinement. The tunability of these materials places them at the forefront of many technologies including displays, <sup>1, 2</sup> light-emitting diodes, <sup>3, 4</sup> and photovoltaics (PVs). <sup>5-7</sup> Over the last few decades, nanomaterial synthesis has advanced substantially, allowing fine control over composition, shape, size homogeneity, and surface passivation with the aim of controlling the properties of the inorganic core. <sup>8-10</sup> Of particular note, many reports have shown that ligands can serve important roles beyond passivation of undercoordinated surface sites and stabilization of colloidal suspension. <sup>11, 12</sup> Surface ligands can directly affect trap state distribution, impact both intra- and interband relaxation, as well as alter

<sup>&</sup>lt;sup>1</sup>Department of Chemistry, Northwestern University, Evanston, IL 60208, USA

<sup>&</sup>lt;sup>2</sup>Institute for Sustainability and Energy at Northwestern, Northwestern University, Evanston, IL 60208, USA

<sup>&</sup>lt;sup>3</sup>McKetta Department of Chemical Engineering, Texas Materials Institute, The University of Texas at Austin, Austin, Texas 78712, United States

<sup>&</sup>lt;sup>4</sup>Center for Nanoscale Materials, Argonne National Laboratory, Lemont, IL 60439, USA

electronic and thermal transport.<sup>12-19</sup> Oftentimes desirable ligands, such as compact inorganic ions, short organic alkanes, or more tightly bound phosphines and thiols, are introduced *via* exchange with the ligand utilized during synthesis in order to achieve such properties.<sup>11, 12, 15, 20, 21</sup>

The I-III-VI semiconductors, such as CuInS<sub>2</sub> (CIS) and CuInSe<sub>2</sub> (CISe), have been hailed as candidates to replace more developed, but toxic Cd- and Pb-based chalcogenide nanocrystals, yet encounter additional complexity with regard to ligand selection.<sup>22</sup> Significant research into these compositions has centered around synthesis and size control, which face particular challenges related to the inclusion of hard (In<sup>3+</sup>) and soft (Cu<sup>+</sup>) Lewis acids.<sup>23</sup> To address this, a variety of ligand precursors have been employed to balance the reactivity of the two metal ions.<sup>23</sup>, <sup>24</sup> At present, CISe NC synthesis is less developed than CIS, but recently, combinations of Seprecursors with different reactivity have allowed tunability of size, shape, and crystal structure (e.g. chalcopyrite vs. zincblende vs. wurtzite). 23,25 Whether intentional or not, CISe NCs can easily be produced in off-stoichiometric ratios and resultant defects are common (i.e. vacancy, interstitial, or antisite defects).<sup>23</sup> The bulk compositions of these materials are marked by a large tolerance for such defects, that when combined with the high NC surface areas offer the potential for a variety of electronic trap states that may significantly reduce carrier transport and light emission. 26-29 Furthermore, the optoelectronic properties such as broad absorption linewidths and large Stokes shifts are often attributed to such defects, the precise identity of which are still under debate. <sup>23, 24,</sup> 30, 31 32

Despite these challenges, CISe NCs have garnered considerable interest owing to near-IR bandgaps of  $\sim$ 1.2 – 1.75 eV for NCs,  $^{23,\,25}$  and 1.01 eV for bulk CISe,  $^{33}$  which are comparable to bulk silicon (1.12 eV). In addition, large scale solution processability enables synthesis of large quantities of monodisperse particles, which is important for engineering commercial devices. Incorporation into PV devices has led to efficiencies of up to 19% for bulk CISe and beyond 22% with the incorporation of small amounts of Ga to form Cu(In,Ga)Se<sub>2</sub>. NCs enable the opportunity to print these materials to achieve flexible devices. High temperature sintering or photonic curing can yield bulk-like thin films while sometimes maintaining nanoscale features.

Towards the goal of solution processed CISe PVs, a variety of different Se-precursors and ligand compositions have been investigated that yield different nascent PV efficiencies. 23, 25, 45-50 The underlying photophysical processes responsible that impact efficiency remain elusive and while CISe NCs are generally believed to behave similarly to CIS, far less research is available for this composition. In this work, we examine CISe NCs passivated with three different ligands commonly used for synthesis of this material, namely oleylamine (OLAm), diphenylphosphine (DPP), and tributylphosphine (TBP). Using transient absorption, distinct spectral features and lifetimes are determined that depend strongly on ligand identity. Photoluminescence (PL) quantum yield (QY) and PV device efficiency mirror these results suggesting that the charge carriers of the inorganic crystalline core are heavily influenced by the ligands, which impart trap states. To determine the nature of these defects, X-ray diffraction (XRD), Raman, and inductively coupled plasma optical emission spectroscopy (ICP-OES) are utilized to study the NC lattices, while FTIR and NMR provide insight into ligand coverage and identity. Taken together, these results suggest a mixture of defects, both within the interior of the NC and at the surface where the ligand composition dictates the predominance of one type of trapping over another. Finally, thermal annealing of the NCs followed with in-situ PL characterization shows heat-induced brightening of the DPP passivated sample with PL at room temperature increasing more than 600% after heating to 600K. Understanding of the role ligands play in both formation and passivation of these

materials along with post-synthetic material processing can offer appreciable benefits for device performance.

# **Results/Discussion**

Three batches of CISe NCs with approximately identical size were synthesized using previously described methods, with additional details provided in the Supporting Information (SI). 43, 51-54 Notably, the main difference between these syntheses is the means of incorporating Se into the reaction mixture. To prepare the first sample, Se was dissolved in OLAm along with other precursors and heated to produce the NCs. For the second and third samples, Se was dissolved in a phosphine-based ligand, *i.e.* DPP or TBP, and injected into the reaction flask at high temperatures. In these later cases, OLAm is still present in the reaction as a solvent. The chemical structures of OLAm, DPP, and TBP are given in Figure 1a along with transmission electron microscopy (TEM) images (1c-f) of the associated NCs (hereafter labeled CISe-X where X is the respective ligand).

Normalized static absorption and emission spectra of the samples in hexanes are given in Figure 1b (solid and dashed lines respectively). As is common with this class of materials, the absorption spectra exhibit features that extend into the NIR with broad linewidths that preclude facile identification of the lowest energy excitonic transition. To distinguish the bandgap energy, we examined the square of the absorption<sup>55</sup> (Figure S3) and found it to be approximately ~1.3 eV for each sample; the absorption that extends to lower energy can be attributed to mid-gap states. PL produced upon excitation of these samples is also broad and appears around 1.0 eV. This large Stokes shift is similarly characteristic of I-III-VI NCs. Similarity in absorption and emission spectra confirm that these samples are nearly identical in size. Given that the emission of all three occurs at the same energy, we can assume that radiative recombination arises from the same electronic state, but that it cannot be due to the conduction to valence band transition owing to the 300 meV difference in energy between absorption and emission.

PLQYs (Figure S2 and Table 1) for the three samples are low (less than 2%), suggesting an abundance of non-radiative trapping that tends to outcompete emission. Despite all samples exhibiting low QYs, an order of magnitude difference from CISe-TBP (1.2%) to CISe-DPP (0.14%) to CISe-OLAm (0.003%) indicates that the prevalence of this trapping is dictated in part by the ligand, either through controlling defect formation in the synthesis or afterwards by passivation of surface sites (or lack thereof). Similar trends are observed when the samples are drop cast as thin film PV devices with CISe-TBP exhibiting the highest efficiency and CISe-OLAm the lowest (Table 1, see SI for more information). The impact of ligand identity here suggests that the NCs capped with TBP offer the longest carrier lifetimes and/or transport carriers much more effectively than the those passivated with DPP or OLAm. From these measurements alone we cannot determine the nature of the electronic states involved in radiative or non-radiative recombination (electron and/or hole traps).

To further characterize the photophysics we used near-infrared transient absorption (TA) spectroscopy. The samples were pumped with an 800 nm laser pulse at a low fluence of j=76  $\mu J/cm^2$ , which produces a comparable average number of excitons (<N>  $\approx$  1) in each sample. TA at other fluences is provided in the SI and does not affect the results discussed here. Transient spectra at time points up to two nanoseconds are given in Figure 2a. Early time traces are dominated by a higher energy ground state bleach and lower energy excited state absorption. As time progresses the bleach shifts to lower energy followed by a reduction in intensity while the

positive signal decays rapidly within the measured spectral window. While the overall shape of the spectra are similar across samples, they evolve over drastically different timescales wherein the CISe-OLAm NCs fully recover within 20 ps, the CISe-DPP NCs within 500 ps, and the lifetime of the CISe-TBP NCs extends beyond the two nanosecond time range measured. To determine lifetimes for the various processes and elucidate their origin, we used a sequential  $A \rightarrow B \rightarrow C \rightarrow D \rightarrow$  Ground model and globally fit the data using nine to ten wavelengths (Figure S5). Further information about fitting along with kinetic traces and population curves are shown in the SI. Fitted time constants appear in Table 1. While  $\tau_1$  (corresponding to the lifetime of  $A \rightarrow B$ ) is similar across the three samples,  $\tau_2$  (State  $B \rightarrow$  State C),  $\tau_3$  (State  $C \rightarrow$  State D), and  $\tau_4$  (State D  $\rightarrow$  Ground), show a strong ligand dependence where CISe-OLAm is the shortest lived, followed by CISe-DPP, and finally CISe-TBP. Figure S9 shows a kinetic trace for the three samples corresponding to the wavelength at the lowest energy bleach (minimum  $\Delta A$  of State C) along with the corresponding fit to demonstrate the stark difference in formation and decay rates across samples.

Despite the difference in ligand identity and resultant rate constants by TA, each sample produced similar evolution associated spectra (EAS) as seen in Figure 2b: (A) a higher energy bleach feature ( $\sim$ 1.24 – 1.37 eV) with an excited state absorption below 1.03 eV, (B), a lower energy bleach ( $\sim$ 1.1 – 1.18 eV) with minimal positive features that decays into (C) a similar bleach that is redshifted by 10-60 meV, (D) a further redshifted bleach (10-60 meV) with significantly reduced intensity before recombining to the ground state. The similarity in linewidth across the bleach features in states B-D suggests that we are chiefly monitoring one population as it moves to different electronic transitions (Figure S8).

From these EAS we can begin to assign the identity of the four states (A, B, C, and D). A previous report on CISe-DPP NCs saw spectral shifting of bleach features and attributed this to intraband relaxation as carriers moved from the 1P state to the 1S state before recombination.<sup>51</sup> However, that study only monitored single wavelength kinetics and the lowest energy bleach that they attributed to 1S was far below that of the bandgap. With global analysis we can separate out the lifetimes and spectra of these four identifiable components. Given the bandgap of ~1.3 eV, our pump is generating hot carriers and therefore we ascribe  $\tau_1$  to intraband relaxation. Reports of ultrafast processes of similar timescales in CIS have been attributed to carrier cooling and more generally, semiconductor NCs are expected to undergo intraband relaxation on the order of hundreds of femtoseconds, which is consistent with our data. 56-60 The lineshapes of States A and B provide evidence of this assignment as well. It is well documented that hot carriers produce derivative-like spectra due to interactions of the pump and probe photons; these biexciton shifts are characterized by a higher energy bleach and an induced absorption that drops in intensity for longer probe wavelengths. 61 State A exhibits this lineshape, while the structure of State B is almost completely negative with evidence of slight absorption at the edge of our detection. We would not expect the ligands to affect intraband relaxation and given the instrument response function for the utilized apparatus (~0.15 ps) these lifetimes are all within error of each other. To further confirm our assignment for  $\tau_1$ , we measured CISe-OLAm samples of varying sizes with 400 nm excitation. Similar to the study on CISe-DPP, we found size affecting the energy of these spectra (e.g. smaller NCs had higher energy bleaches and absorptions). For the smallest NCs we were able to resolve the absorption features changing shape with time, from that of a derivative-like biexciton shift towards an induced absorption that increased in intensity towards redder wavelengths as one would expect of a bandedge exciton experiencing intraband transitions (Figures S14-15).<sup>62</sup> Furthermore, we find that the dynamics for carrier cooling are slightly elongated (0.2 - 0.6 ps) when samples

are excited with higher energy photons, consistent with carriers dissipating more energy upon relaxation through more electronic states.

From the TA alone, the nature of States C or D are not immediately apparent. We can rationalize that none of the states measured are emissive as they are all too high in energy. In addition, the low PLQY suggests that only small fractions of carriers are meaningfully populating the emissive state, suggesting that any TA signals that correspond to radiative recombination are overwhelmed by non-radiative ones. We note that a shift in bleach signals has been noted in other compositions of semiconductor NCs, namely quantum-confined InSb. In that case it was due to a multiple conduction band valleys, <sup>63</sup> which is not likely the source of our signals due to the band structure of CISe. There have been several reports that the electrons may trap at surface states on these timescales, <sup>31, 58</sup> and there is also literature precedence for intrinsic electron and hole traps. <sup>23, 25, 30</sup>

XRD and Raman (Figure 3) were employed to probe the crystallinity of our samples and offer insight into defect states that could serve as carrier traps. XRD confirms that all three samples exhibit the chalcopyrite crystal structure. At first glance there are no discernable differences between the diffraction data. Slight broadening in the **CISe-DPP** sample can be attributed to size distribution (*i.e.* Scherrer broadening), but the position and amplitude of all peaks are consistent. Upon closer inspection there is a weak feature around 35.6°, most evident in the **CISe-TBP** sample, that corresponds to the (211) reflection. The lack of this feature has been attributed to cation disorder and point defects within the crystalline lattice, namely ordered vacancy defect pairs of indium copper antisites (In<sub>Cu</sub><sup>2+</sup>) and copper vacancies (V<sub>Cu</sub><sup>1-</sup>).<sup>64</sup> It is also seen in In-rich thin films of CISe, which is consistent with the aforementioned defects.<sup>65</sup> The **CISe-OLAm** sample is lacking this feature whereas it is weakly present in the **CISe-DPP** NC diffraction.

Raman spectra of the samples also show nearly identical features for the three different NC-ligand compositions. The strong signal at  $\sim 180~\text{cm}^{-1}$  corresponds to the  $A_1$  vibrational mode of the CISe lattice. The higher energy feature at 230 cm<sup>-1</sup> has previously been used as a benchmark for point defects such as  $V_{\text{Cu}}^{1-}$  and  $In_{\text{Cu}}^{2+}$  in CISe NCs synthesized with OLAm. He observe that this feature is prevalent in all three samples with similar amplitudes. Fitting of the peaks provides a more quantitative ratio between the two modes (Figure S31). **CISe-DPP** displays the weakest proportion of the defect state with **CISe-OLAm** and **CISe-TBP** showing nearly identical proportions (Table 1). We note that this analysis is potentially complicated by a lower-energy feature around  $\sim 115~\text{cm}^{-1}$  which also arises from defects. Due to limited range on our Raman spectrometer we cannot resolve this feature or completely deconvolute contributions from Rayleigh scatter. Despite this, the intensity of the lower wavenumber mode shows similar behavior to the 230 cm<sup>-1</sup> defect feature with more intensity for **CISe-OLAm** and **CISe-TBP**. The features at higher wavenumbers correspond to phonon overtones and were too noisy to fit individually.

CISe NCs can easily be synthesized in off-stoichiometric rations, Cu- or In-rich are particularly prevalent and can lead to distinct photophysical properties due to inclusion of different midgap electronic states. <sup>26</sup> ICP-OES analysis was used to determine the ratio of Cu:In present in our samples. We find that the CISe NCs are In rich and while **CISe-OLAm** and **CISe-DPP** exhibit very similar ratios (Cu/In  $\approx$  0.94), **CISe-TBP** has an increased amount of In present (Cu/In  $\approx$  0.81). These experiments were run in triplicate to ensure that any differences between samples are statistically determined (see SI for further details). This result suggests that the ligands directly impact the stoichiometric composition of the NCs during synthesis, likely due to differences in reactivity with Cu and In precursors. Ligands have been known to change the prevalence of Cd or Se on the surface of CdSe NCs, but oftentimes the core of cadmium chalcogenide NCs are not as

drastically affected by ligands.<sup>67, 68</sup> The increased complexity of ternary materials such as CISe and CIS present a higher likelihood of non-stoichiometric compositions such that they are impacted strongly by the reactivity of the ligand.

With this information we can determine the identity of States C and D from TA. A wide range of defects are known to produce energy levels within the bandgap of CISe, however In-rich CISe is predominately characterized by pairs of  $In_{Cu}^{2+}$  and  $V_{Cu}^{1-}$  defects to produce the offstochiometric ratio. State C is approximately 15-60 meV below that of Species B. Given the lighter nature of the electron we can assume that the TA is mostly monitoring its movement to a new state. In this case the energy gap corresponds well with the difference in conduction energy levels and  $In_{Cu}^{2+}$  antisite defects, which are known electron traps. Species C and D have nearly the same half-width half max (HWHM) suggesting the same population moving together to a slightly lower energy state. The energy difference (10-40 meV) matches well with the energy gap between the valence band and  $V_{Cu}^{1-}$ , commonly thought to be hole traps in CISe. Reduction in bleach signal intensity is consistent with depletion of band-edge states (both conduction and valence band) so despite the hole not being as evident in TA, the opening of the bandgap transition and loss of bleach is noticeable.

Despite being able to characterize the identity of these defects, recombination of a localized electron and hole from these trap sites must be non-radiative. From the TA, we know that neither of these states are low enough in energy to correspond with PL, nor is this type of recombination (donor-acceptor model) consistent with reports of size dependent PL for CISe. <sup>70, 71</sup> Given the low proportion of population that radiatively recombines we are likely not seeing the emissive state by TA. Instead, we propose that it is occurring from  $Cu^+/Cu^{2+}$  defect couples that are theorized to be the radiative pathway in CIS NCs. These defects have been shown to produce broad emission and a  $Cu^{2+}$  can be paired with a  $V_{Cu}^{1-}$  to still produce In-rich CISe. It is hotly debated the origin of these defects and their role in the radiative process, for example whether the  $Cu^{2+}$  is an intrinsic defect or formed from a photogenerated hole recombining with a  $Cu^+$  ion and whether the  $Cu^{2+}/Cu^+$  defects occupies a lattice position or are interstitial defects. <sup>72-75</sup>

To understand non-emissive trap states further, we performed temperature dependent PL at both cryogenic and elevated temperatures (Figure S23). Both CISe-OLAm and CISe-TBP samples exhibited similar behavior, with increased PL intensity as the temperature was lowered to 80K and decreased PL at elevated temperatures. Similar results have been found in a variety of semiconductor nanocrystals such as CdSe, Si, InP, and CuInS<sub>2</sub>.<sup>74, 76-79</sup> The CISe-DPP sample similarly showed higher PL at low temperatures. Upon heating, it began to brighten, a trend that continued with rising temperature. After returning to 290K the sample remained brighter. To ensure that this increase was not due to photobrightening from the laser, the sample was moved to fresh spots. While PL intensities differ due to film thickness, all showed at least twice the PL intensity found before heating (Figure S24).

To further study the origin of this brightening in the CISe-DPP sample, we performed a pendulum (cyclic) heating experiment where the temperature was raised incrementally with consistent returns to room temperature to examine PL intensity and lineshape (Figure 5a,b). Initial heating from 290K to 400K and back increased the PL intensity by 115%. Heating to 500K and 600K further increased PL by 188% and 623% respectively. A return to 600K caused the PL intensity of the film to drop. Throughout the pendulum experiment, we observed no shift in the spectral maximum of the PL at room temperature suggesting that no sintering was occurring. Since the lineshape and peak did not change during these experiments, we are monitoring the same

emissive state as before, but are either increasing its prevalence or reducing competing non-radiative pathways.

Raman and TA (measured at room temperature) were used to examine CISe-DPP film duplicates that were removed following thermal treatment at 400, 500, and 600K as well as a final increase to 600K. Results from Raman spectroscopy are summarized in Figure 5c. Interestingly, an increase of the higher wavenumber Raman feature (230 cm<sup>-1</sup>) is observed as the temperature is increased with the highest increase occurring in the single 600K ramp experiment. This suggests that not only does this feature provide information about  ${\rm In_{Cu}}^{2+}$  and  ${\rm V_{Cu}}^{1-}$  defects, but also the Cu<sup>+</sup>/Cu<sup>2+</sup> couple. TA lifetimes upon heating show differences in lifetimes and lineshapes (Figure S25 and Table S5) and although a clear trend in time constant is not evident, a reduction in the amplitude of State C occurs consistently with each ramp cycle.

To probe changes in the core structure, another heating cycle experiment was performed on a film of CISe-DPP NCs while monitoring changes in room-temperature XRD (Figure S26). After heating to 450K and 600K, peak width did not change appreciably overall, suggesting the size of the particles remained constant, which is consistent with the lack of discernible change in PL emission energy. Peak intensity, however, was affected by thermal annealing, with peaks at higher 2θ growing in amplitude. We attribute this behavior to an increase in order in the crystal structure at shorter distances, potentially *via* removal of grain boundaries, loss of impurity crystal phases, or surface reorganization. 80-83 A report on annealing in CISe-OLAm NCs saw that at much higher temperatures (~870K) there was a decrease in the defect Raman feature and increase in the (211) diffraction peak which they attributed to reduction of defects. 64 In our experiment on CISe-DPP NCs we did not observe an increase in the (211) feature after heating, which suggests a different process is occurring or that higher temperatures may change the crystal structure substantially. Since we saw a reduction in PL of the CISe-DPP sample upon multiple ramps to 600K as well as sintering in the CISe-TBP after heating the balance between ligands, surface, and intrinsic defects is delicate and highly dictated by the temperature.

Lastly, we turn to techniques that are sensitive to the organic ligands, namely FTIR and NMR to better understand surface passivation in these materials. Figure S27 shows the FTIR spectra of the NCs along with the corresponding spectra of the ligands alone. All samples show strong OLAm features around 2850 and 2925 cm<sup>-1</sup>, which is not surprising since all NCs were synthesized in the presence of OLAm. The **CISe-DPP** and **CISe-TBP** samples do show IR bands associated with their respective phosphine ligand, suggesting that it is present to some degree. Importantly, FTIR is sensitive to all molecular species present regardless of whether they are bound to NC surfaces. Since these samples were cleaned and purified *via* multiple centrifugation steps (see SI), it is unlikely that the signal would be dominated by excess ligands.

We utilized NMR spectroscopy to differentiate bound vs. free species and quantify the ligand density, these results are summarized in Figure 5. Signals broaden and shift downfield when a molecule is bound to a particle compared to one freely moving in solution. While OLAm has a large variety of peaks between 0 and 3 ppm that are spectrally dense and complex to interpret, the region between 5-6 ppm (corresponding to the alkenyl hydrogens) is less populated and has commonly been used for analysis. A broad feature around 5.6 ppm is evident in all three samples suggesting that OLAm is in fact bound to the surface in all cases. A sharper feature at 5.4 ppm corresponds to free OLAm in solution and confirms our hesitation from FTIR in assuming all signals are due to bound species.

In the case of **CISe-DPP** (red trace), features above 7 ppm (panel b) match the expected proton shift of the phenyl protons. Here the signals are complicated due to multiplicity and various

confirmations possible for this ligand as well as strong features from trace toluene solvent protons. In addition, other work has shown that a disubstituted phosphine such as DPP can react with a primary amine during the synthesis of NCs, which will likely present different NMR signatures. Regardless the region around 8 ppm was fit to determine the ratio of DPP:OLAm ligands bound on the surface. From this analysis we determine that DPP constitutes approximately ~18% of bound ligand. Fits and further explanation are provided in the SI.

Similar analysis was performed for CISe-TBP. The prevalence of alkanyl hydrogens on this ligand means that its signals are almost completely obscured by those of OLAm. However, a discernable feature at 0.9 ppm corresponds to the terminal protons of TBP, which is not present in the other samples (panel c). Fitting of this feature again provides a rough estimate of the ratio of TBP to OLAm, which we find to be ~11%. These results are summarized in Table 2. We furthermore calculated the ligand density on the surface of the NCs using CH<sub>2</sub>Br<sub>2</sub> as an internal standard. An average of 1.5 - 1.8 ligands/nm<sup>3</sup> was determined for these samples, which is lower than most measurements of ligand density on NCs.<sup>84, 86</sup> While OLAm is bound to the surfaces of all three samples, increase in both the ligand density and the appearance of bound phosphines in the CISe-DPP and CISe-TBP points to passivation of additional surface states. One of the features of this class of ternary materials is the combination of hard/soft Lewis acids/bases. In the case of CISe, Cu<sup>+</sup> is a soft Lewis acid while In<sup>3+</sup> is a hard Lewis acid. As mentioned above we also argue the incorporation of Cu<sup>2+</sup> defects, which serves as an intermediate Lewis acid. Furthermore, OLAm is known to be a hard Lewis base and TBP, a soft base. DPP likely falls in between based on its pK<sub>a</sub> values.<sup>87</sup> Given the differences in basicity between these ligands we can assume they are binding to different surface sites (In vs. Cu). We cannot overlook the trend in basicity that matches much of our results above and potentially points to stability of certain reaction intermediates or surface states.

From these results it is clear that surface trapping serves as an additional source of non-radiative pathways in all these samples, but particularly **CISe-OLAm** since it lacks a phosphine-based ligand and is unable to passivate both types of metals. This is supported by studies on both CIS and CISe NCs with different ligand compositions where amines were found to produce poor surface passivation while phosphines were better.<sup>32, 88</sup> This comparison is complicated by the studies primarily focusing on post-ligand exchange which can cause deterioration of the surface.<sup>89, 90</sup>

With all of these results we can now build a picture of the complicated photophysics of this system, which we have summarized in Figure 6. OLAm, DPP, and TBP act during the synthesis to change the ratio of In/Cu within the NCs, afterwards they passivate specific surface states. In the end, the NCs have a variety of different traps and the number of each kind determines the probability of a carrier localizing on the surface or in an internal defect. Localization at  ${\rm In_{Cu}}^{2+}$  and  ${\rm V_{Cu}}^{1-}$  defects is non-radiative and competes with the slower radiative process wherein a delocalized electron recombines with a localized hole.

# **Conclusions**

There are two main mechanisms from which ligands can cause drastic changes in photophysical behavior, namely incorporation of defects within the crystalline lattice upon synthesis of the materials or poor passivation of trap states at the surfaces. Here, ligands play a direct role in both the synthesis of the NCs *and* passivation of the surfaces afterwards. In this study we examined the effects that the synthetic ligand/Se-precursor has on the photophysical, structural, and temperature dependent properties of CISe NCs. The inorganic crystal and the organic ligands

must be considered as an entire system given the drastic changes they can have on optoelectronic properties. We found that differences in Cu:In ratios, defects within the lattice as well as complex surface-ligand bonding are contributing to the properties seen here. Depending on the ligand present localization at  $V_{\text{Cu}}^{1}$ -/In<sub>Cu</sub><sup>2+</sup> defects or undercoordinated surface metal ions can prevent radiative recombination that occurs at  $\text{Cu}^{2+}/\text{Cu}^{+}$  couples. Using an amine based ligand (OLAm) produces the highest quantity of trap states and resulted in very short lifetimes and PLQY. Phosphine based ligands (DPP, TBP) reduced the prevalence of surface trapping, but produced stark differences in the Cu:In ratio depending on the identity of the phosphine. Thermal annealing at 600K of CISe-DPP produced a 600% increase in PLQY suggesting a post-synthetic mechanism for increasing emission intensity. This effect likely arises due to increased crystalline order, although not removal of all defects as these are still observed by Raman and XRD.

Future studies of new Se-precursors may produce NCs with longer charge separation lifetimes that prove to be better in photovoltaic applications. Different amine and phosphine compositions with varying basicity, sterics, and reactivity can be employed to expand understanding of the complex role that ligands play during synthesis by affecting their affinity for Cu and In, thus possibly affording control over product stoichiometry ratios. The interaction of disubstituted phosphines with primary amines adds another parameter to the synthesis, but one that may prove beneficial if understood for CISe as it is for CdSe. 85 Thiols, another soft Lewis base, is oftentimes used in the synthesis of CIS NCs and has been found to produce higher PLQYs than phosphines suggesting that the surface of these materials are very sensitive to the ligand and also highlights the importance of HSAB theory for proper alignment of ligand and surface reactivity.<sup>25</sup>, <sup>91</sup> Thiols are less commonly used in the synthesis of CISe NCs due to formation of CISSe hybrid structures, precluding direct comparison. <sup>91</sup> The reduction of trapping with shells in both CIS and CISe NCs has been reported by a variety of groups and may reduce some non-radiative surface sites.<sup>30</sup> However, the ligands present in those studies are not the same as the ones here and a direct comparison should not be made. Shelling of nanocrystals can also lead to incorporation of the shell composition's cation due to diffusion or alloying at the surface, potentially changing the electronic structure of the material.<sup>30</sup> Further studies that add shells to NCs with these three ligand compositions would need to be undertaken to determine the extent of surface trapping. To enable better understanding of emission, spectroelectrochemistry and magneto-optical experiments, similar to what has been done for CIS, are needed to unravel the nature of the Cu<sup>+</sup>/Cu<sup>2+</sup> couple.<sup>72-</sup>

# Methods/Experimental

# Materials

Copper(I) chloride (CuCl, 99.99%), indium chloride (InCl<sub>3</sub>, 99.99%), selenium powder (Se, 100 mesh, 99.99%), anhydrous toluene (99.8%), oleylamine (OLAm, ≥ 98%) tributylphosphine (TBP, 97%), and diphenylphosphine (DPP, 98%) were purchased from Sigma-Aldrich. Toluene (ACS reagent, ≥99.5%) and ethanol (anhydrous, ACS/USP grade), and ammonium hydroxide (NH<sub>4</sub>OH, 18 M) were purchased from Fisher Scientific. Cadmium sulfate (CdSO<sub>4</sub>, ≥99.99%), and thiourea ((NH<sub>2</sub>)<sub>2</sub>CS, ≥99%) were obtained from MilliporeSigma. OLAm was degassed before use by maintaining vacuum under 200 mTorr for 4 h at 110 °C and then stored in a nitrogen-filled glovebox. All other chemicals were used as received.

#### **CISe-OLAm Synthesis**

In a N<sub>2</sub>-filled glovebox, 40 mL OLAm, 5 mmol (0.49 g) CuCl, 5 mmol (1.11 g) InCl<sub>3</sub>, and 10 mmol (0.79 g) Se were added to a 100 mL three-neck flask. The flask was sealed with septa and wires, transferred out of the glovebox to connect to a Schlenk line. The reaction mixture was heated to 110 °C under vacuum (<200 mTorr) for 1 h, followed by blanketing with N<sub>2</sub> for 12 h to allow the precursor complexes to form completely. Then the reaction was carried out at 240 °C for 10 min. The heating mantle was then removed to allow the reaction mixture to cool down to room temperature. CuInSe<sub>2</sub> nanocrystals were purified through antisolvent precipitation, by addition of 20 mL ethanol and centrifugation at 2600 rcf for 5 min. After discarding the supernatant, the nanocrystals were redispersed in 10 mL of toluene and centrifuged again at 2600 rcf to remove poorly capped nanocrystals. The supernatant was transferred to another centrifuge tube, and one more antisolvent precipitation steps was carried out. Ethanol (4mL) was added, followed by centrifugation at 2600 rcf for 5 min, and the supernatant was discarded. The collected nanocrystals were dried and redispersed in anhydrous toluene, stored in the glovebox.

# **CISe-DPP Synthesis**

In a N<sub>2</sub>-filled glovebox, 40 mL OLAm, 5 mmol (0.49 g) CuCl and 5 mmol (1.11 g) InCl<sub>3</sub> were added to a 100 mL three-neck flask. The flask was sealed with septa, removed from the glovebox, and transferred to a Schlenk line. The reaction mixture was degassed under vacuum (<200 mTorr) at 110 °C for 30 min, followed by blanketing with N<sub>2</sub> at 110 °C for another 10 min. The flask was then heated to 240 °C; at 180 °C, Se-DPP solution, prepared from dissolving 10 mmol (0.79 g) Se by 10 mL of diphenylphosphine in the glovebox, was injected into the flask. The flask was maintained at 240 °C for 10 min. Then the heating mantle was removed to allow the reaction mixture to cool down to room temperature, and CuInSe<sub>2</sub> nanocrystals were purified by the same procedures in the CISe-OLAm synthesis above.

# **CISe-TBP Synthesis**

CISe-TBP synthesis was performed following the same steps as CISe-DPP synthesis, expect that 10 mmol (0.79 g) Se was dissolved in 10 mL of tributylphosphine.

# **Transient Absorption**

Transient absorption measurements have been described previously. Briefly, the 800 nm output of a 35 fs, Ti:sapphire laser operating at 2 kHz was chopped at half the repetition rate and served as the pump source. A small portion of the beam was portioned off before the chopper and focused through a sapphire crystal to generate near-infrared white light for the probe. Absorption spectra were collected and differenced (pump on minus pump off). Samples were run as dilute solutions (0.1 - 0.3 OD at excitation wavelength) or as films when comparing to temperature dependent PL.

#### **Photoluminescence**

Nanocrystals were excited at 808 nm and static PL spectra were collected using a liquid nitrogen cooled ingas array detector. For determination of the quantum yield, samples were diluted in a cuvette to ~0.2 OD at the excitation wavelength and compared to the standard IR26 dissolved in tetrachloroethylene. <sup>93</sup>

# **Temperature Dependent Photoluminescence**

Samples were diluted in hexanes and dropcast onto a glass coverslip. The film was mounted in a vacuum cold finger cryostat and cooled using liquid nitrogen. Samples were excited using a 532

nm laser diode and PL spectra were collected using a fiber optic and a liquid nitrogen cooled ingas array detector. At higher temperatures dark spectra (without laser excitation) were collected and subtracted from the data as blackbody radiation was evident.

# **Raman Spectroscopy**

Dropcast films of each sample were excited with either a 532 nm or 633 nm laser diode. Raman spectra were collected using a Renishaw inVia confocal Raman microscope. Multiple spots were measured with 20 second integration to ensure that the sample was not impacted by photoexcitation.

# X-Ray Diffraction

Powder X-ray diffraction (XRD) data were acquired using a Rigaku R-axis Spider Diffractometer with an image plate detector. Cu K $\alpha$  ( $\lambda$  = 1.54 Å) radiation was used with 40 kV and 40 mA power supply. Dried powder is suspended in a 0.5 mm nylon loop. The samples are scanned for 10 min while rotating at 1°/s. The diffraction patterns are integrated with the Rigaku 2DP powder processing program.

#### **FTIR**

FTIR spectra were collected in nitrogen on dropcast films using a KBr substrate. Background spectra were collected and subtracted.

#### **NMR**

To prepare samples for NMR a large suspension of CuInSe $_2$  nanocrystals was dried under nitrogen and then redispersed in 0.6 mL of deuterated toluene. 2  $\mu$ L of CH $_2$ Br $_2$  was added to each NMR tube to serve as the internal standard. Samples was run on a Bruker Avance III 600 MHz spectrometer. Afterwards a small amount was carefully diluted, and an absorption spectrum was measured to determine the concentration of nanocrystals in solution.

#### **Transmission Electron Microscopy**

Samples were diluted until solution was barely colored and dropcast onto copper TEM grids. Nanocrystals were imaged using a JEOL JEM-2100F operated at 200kV.

#### **ICP-OES**

Samples were prepared for ICP-OES analysis using the following procedure. To begin, a stock solution of nitric acid was prepared by diluting fuming HNO<sub>3</sub> (90%) to a concentration of approximately 30% (solution changed from bright yellow to very pale or completely clear). A small amount of the dried nanocrystals were added to a vial (1-20 mg) and 6 mL of the HNO<sub>3</sub> solution were added. Sonication was used to dissolve as much solid material as possible and the resulting suspension changed from brownish black to red-orange. Since a large quantity of solid material remained 2 mL of HCl (37%) were added to the vials. Solution immediately become more orange-yellow. Samples were sonicated again and then left uncapped overnight to allow further dissolution. The next day the solution had turned a pale yellow and no remaining solids could be seen. 1 mL of this solution was diluted with 9 mL of deionized water in a centrifuge tube. Three tubes were prepared for each sample (CISe-OLAm, CISe-DPP, and CISe-TBP) along with three blanks that only included HNO<sub>3</sub>, HCl, and DI water to ensure that no trace amounts of metal impurities were detectable. Errors reported in Table 2 are statistically calculated. Samples were

run by staff scientist at the Quantitative Bio-Element Imaging Center at Northwestern. Ratios of Cu, In and Se are given in Table S1 normalized to Se.

#### **Device Fabrication and Characterization**

Polished soda-lime glass substrates (25 x 25 x 1.1 mm) purchased from Delta Technologies were cleaned before thermal evaporation of the chromium (Cr) and gold (Au) layers, by placing in an ultrasonic bath of 1:1 vol% acetone: isopropanol for 5 min, followed by 5 min of sonication in DI- $H_2O$  (resistivity as 18.2 M $\Omega$ -cm at 25 °C), and drying with compressed air. Cr (10 nm) and Au (80 nm) layers were deposited in a Denton thermal evaporator through a patterned mask. 94 A Sonotek ExactaCoat ultrasonic automated spray system was used to deposit CuInSe<sub>2</sub> nanocrystals (dispersed in toluene at a concentration of 5 mg/mL), equipped with a 120 kHz ultrasonic nozzle, rastering across the substrates with a 3 mm raster spacing, at a speed of 10 mm/sec, an ink injection rate of 0.1 mL/min, an air pressure of 1.6 psi and a nozzle-to-substrate height of 11.5 cm. The substrates were heated to 100°C prior to spray coating. 95 The CdS device layer was deposited onto the nanocrystal films through a chemical bath deposition (CBD) process. 96 Aqueous solutions of 160 μL of 15 mM CdSO<sub>4</sub>, 275 μL of 1.5 M thiourea, and 350 μL of 18 M NH<sub>4</sub>OH were mixed and dropped onto each substrate maintained at 90°C. The substrates were covered with a glass dish for 2 min, then rinsed with DI-H<sub>2</sub>O and dried with compressed N<sub>2</sub>. Layers of intrinsic ZnO (50 nm) and ITO (300 nm) were deposited in a AMOD Sputtering system through Radio Frequency (RF) sputtering in Ar atmosphere, using ZnO (99.9%) and ITO (In<sub>2</sub>O<sub>3</sub>:SnO<sub>2</sub> 9:1, 99.99%) targets supplied by Kurt J. Lesker. The sputter deposition area was shadow-masked into 8 rectangular regions corresponding to 8 individual devices on each substrate. The active device area varies slightly from 0.08 cm<sup>2</sup> to 0.11 cm<sup>2</sup>, and was measured in each case to determine all reported power conversion efficiencies (PCE).

Current-voltage characteristics of the PVs were measured with a Keithley 2400 general purpose source meter and a Xe lamp equipped with an A.M. 1.5 filter. Conductive silver paint (SPI Supplies) was applied to make contact between the ITO layer and the electrical probes.

#### **Supporting Information**

Supporting Information is available free of charge on the ACS Publications website at DOI... Further analysis of TA spectra, kinetic fits, and power dependent data. CISe-OLAm size dependent TA, fitting, and analysis. Temperature dependent PL experiments along with room-temperature TA and XRD of resulting films. Data including FTIR, Raman, TEM sizing histograms, NMR fitting process and J-V curves. Explanation of how the bandgap was determined for each sample.

#### Acknowledgements

S.M.H. gratefully acknowledges funding from the National Science Foundation Graduate Research Fellowship under Grant DGE-1842165. We acknowledge support of the National Science Foundation under MSN-1808950. This work was performed, in part, at the Center for Nanoscale Materials, a U.S. Department of Energy, Office of Science User Facilities, and supported by the U.S. Department of Energy, Office of Science, under Contract DE-AC02-

06CH11357. This work was supported by the U.S. Department of Energy, Office of Science, Office of Basic Energy Sciences under Award DE-FG02-99ER14999 (M.R.W.). D. W. H., W. L., and B. A. K. acknowledge the Robert A Welch Foundation (F-1464), the Industry/University Cooperative Research Center on Next Generation Photovoltaics (IIP-1540028), and the Center for Dynamics and Control of Materials (CDCM) Materials Research Science and Engineering Center (MRSEC) (DMR-1720595). This work made use of the IMSERC NMR facility at Northwestern University, which has received support from the Soft and Hybrid Nanotechnology Experimental (SHyNE) Resource (NSF ECCS-1542205), Int. Institute of Nanotechnology, and Northwestern University. The authors would like to thank B. Sponenburg for running the ICP-OES experiment. Metal analysis was performed at the Northwestern University Quantitative Bio-element Imaging Center.

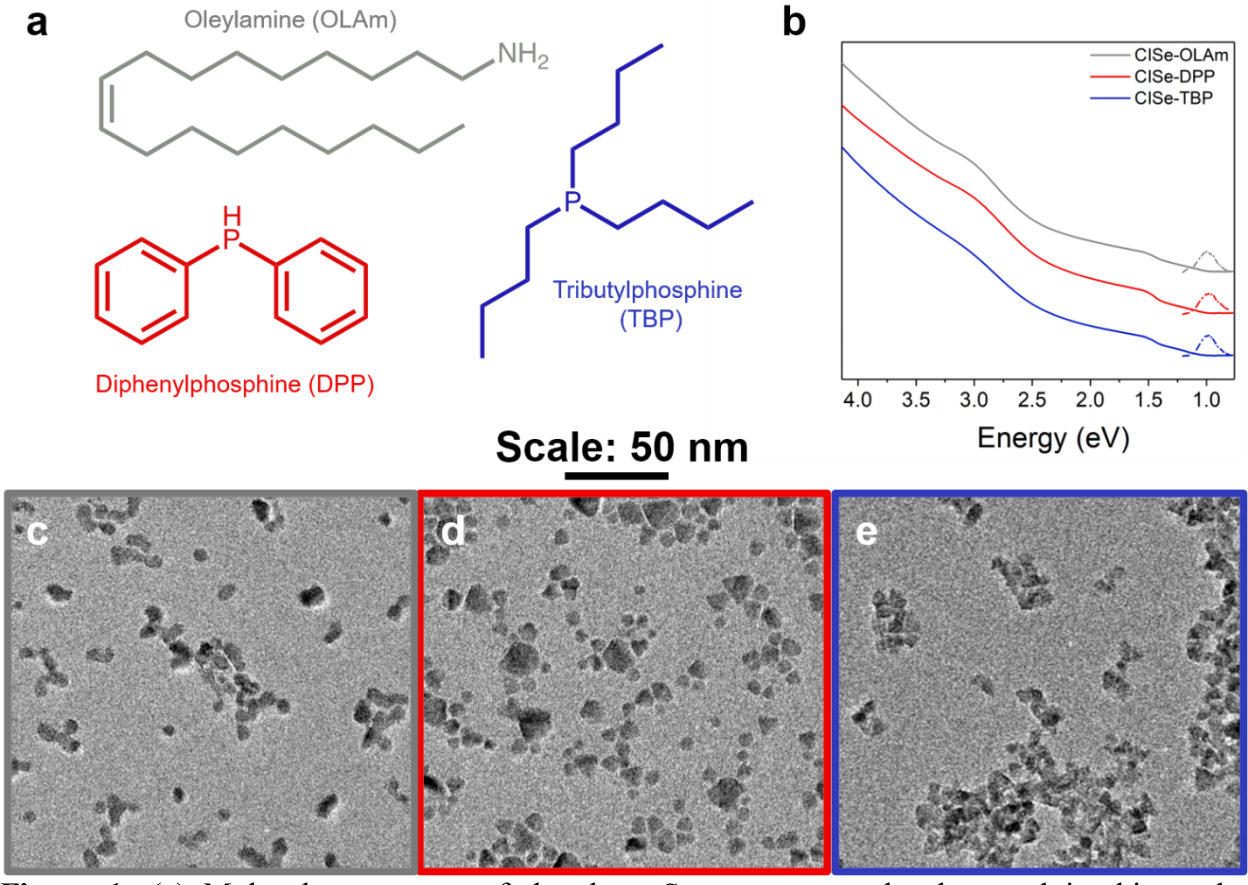


**Figure 1:** (a) Molecular structure of the three Se-precursor molecules used in this study, oleylamine (present in all three samples), diphenylphosphine, and tributylphosphine. (b) Static absorption spectra (solid lines) and photoluminescence (dashed lines) of the CISe NCs. (c-e) Transmission electron microscopy images of the samples synthesized from left to right with OLAm, DPP, and TBP. Scale bar is the same for all three.

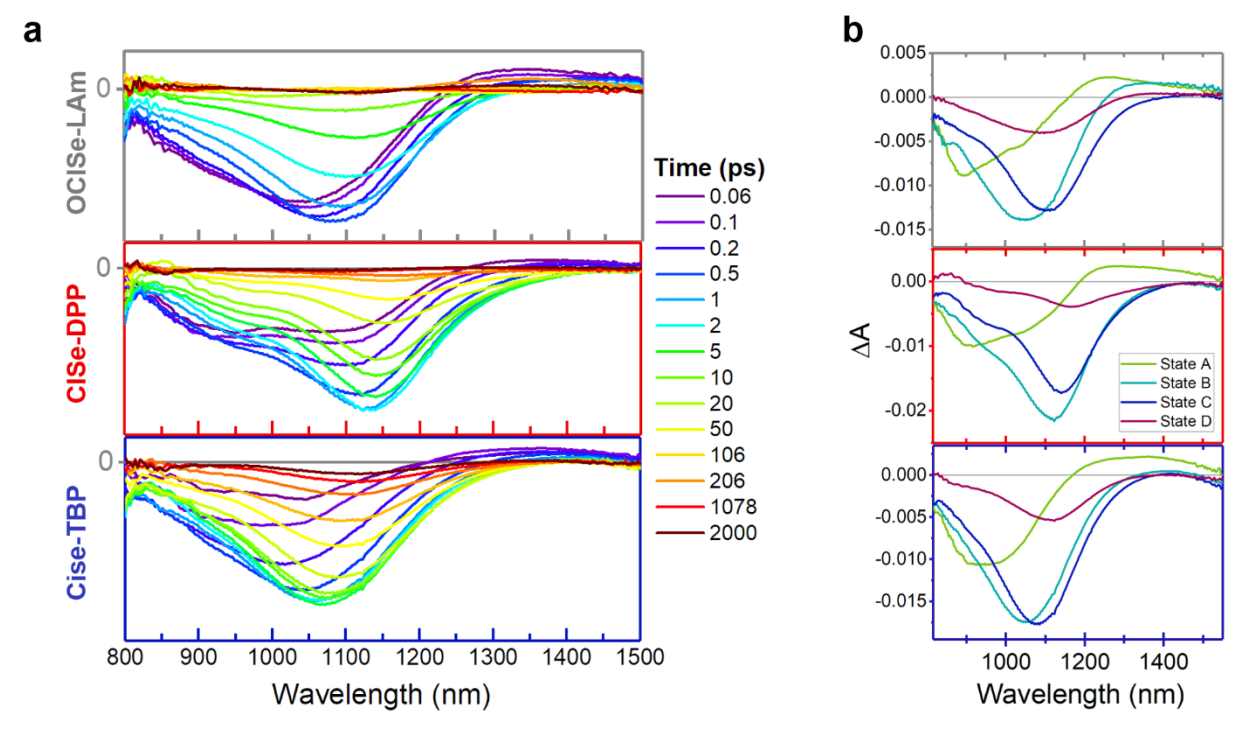


**Figure 2:** Transient absorption data. (Left) Transient spectra for each sample up to 2 ns. (Right) Evolution associated spectra determined from fitting the data using a three species model.

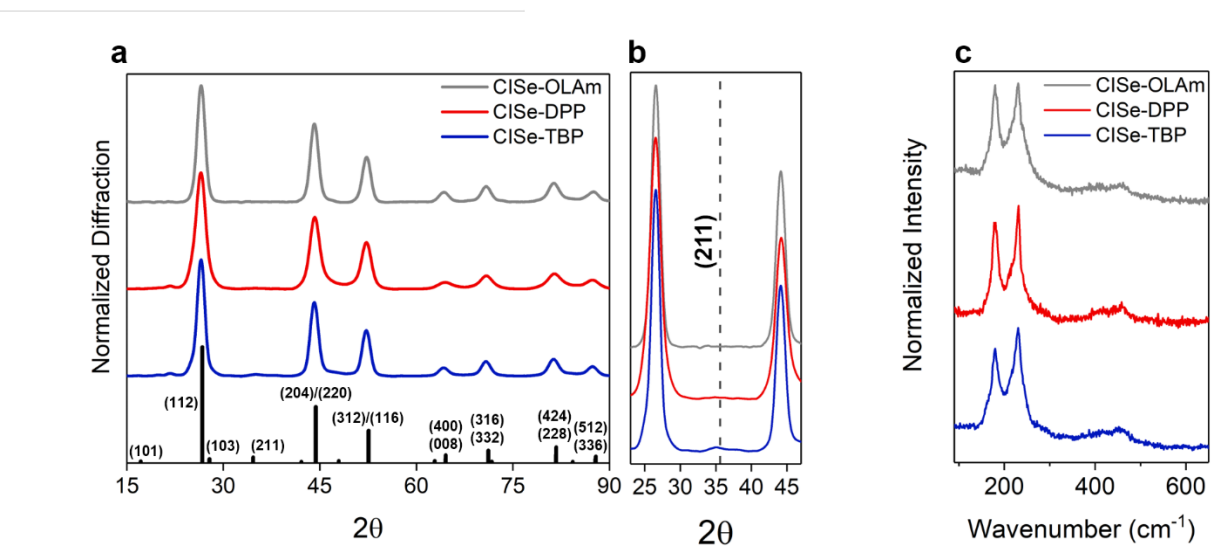


**Figure 3:** Investigation of the CISe crystalline lattice. (a) X-ray diffraction of all three samples showing the chalcopyrite crystal structure. (b) Slice of the XRD focusing on the (211) feature at 36° (c) Raman spectra display features around 180 and 230 cm<sup>-1</sup>. The low intensity peaks between 300 and 500 cm<sup>-1</sup> are second order features.

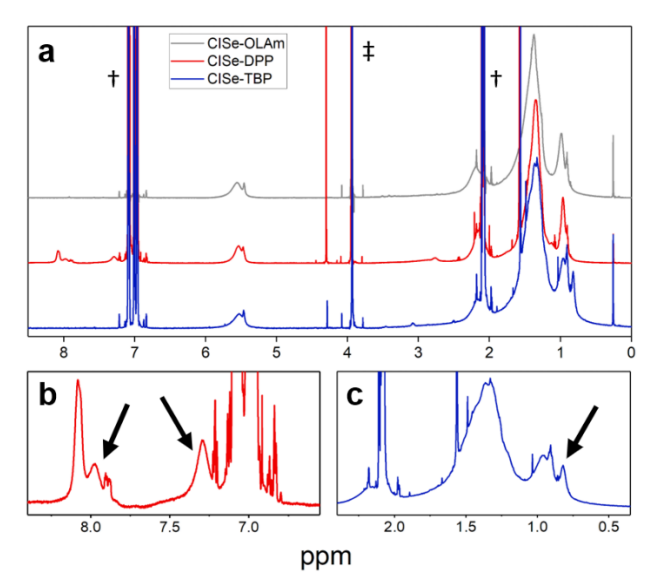


**Figure 4:** NMR of the three samples. The broadened feature around 5.6 ppm corresponds to the alkenyl hydrogens of oleylamine. † denotes toluene features while ‡ is from CH<sub>2</sub>Br<sub>2</sub> used as a standard to calculate ligand concentration. (b) and (c) are insets showing features corresponding to bound DPP and TBP respectively.

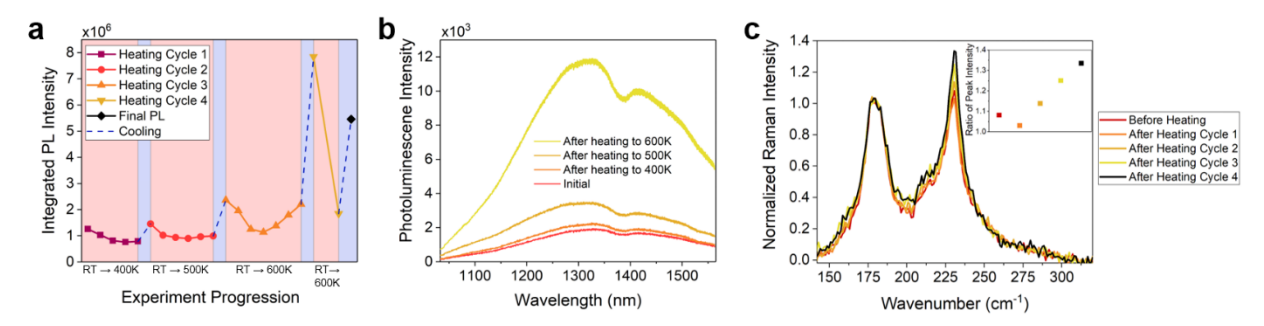


**Figure 5:** Pendulum heating of the CISe-DPP sample. The sample underwent a total of four heating cycles, from room temperature to 400, 500, 600K with intermittent steps and a final ramp from room temperature to 600K and back to room temperature. (a) Integrated PL intensity during the heating cycles (dashed connector signifies cooling from the highest indicated temperature back to room temperature). (b) PL spectra of the sample initially and after the first three heating cycles. (c) Portions of the sample were removed after each heating cycle and examined using Raman spectroscopy. An increase in the 230 cm<sup>-1</sup> feature occurred after heating to higher temperatures.

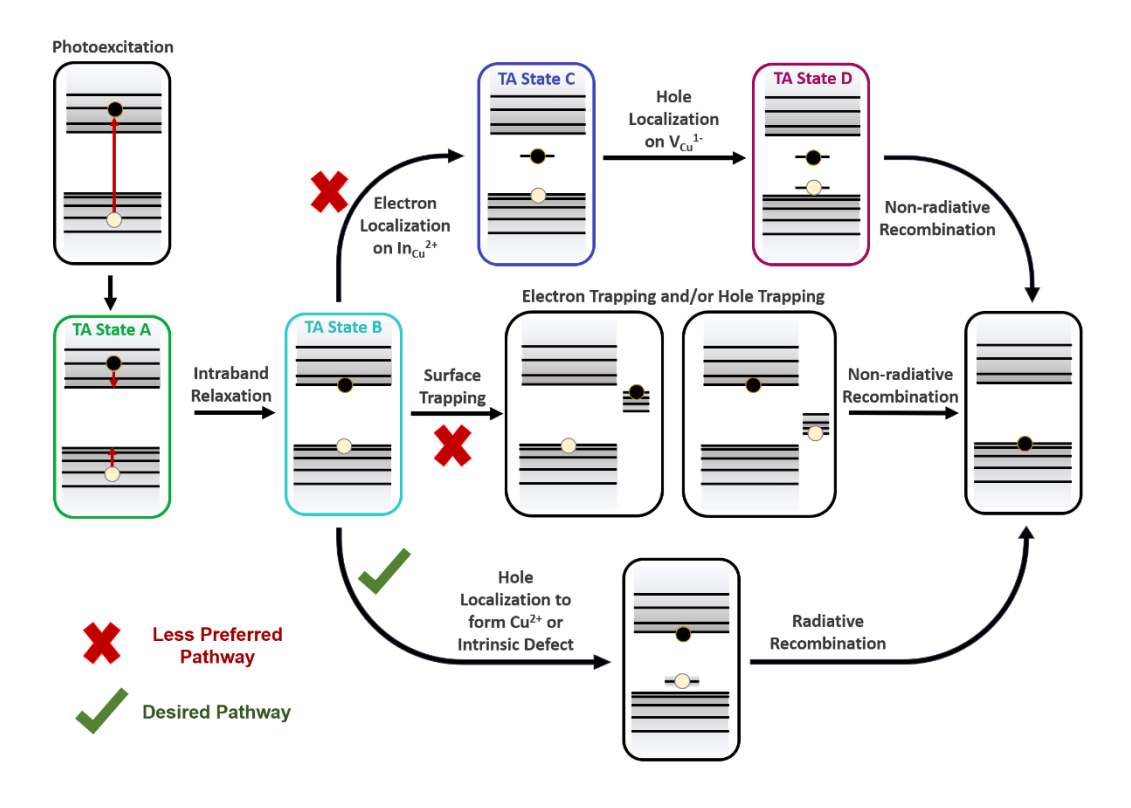


**Figure 6:** Diagram showing the different electronic states involved in carrier processes in CISe NCs. After excitation, electrons and holes undergo intraband relaxation followed by intrinsic trapping or surface trapping. Localization at intrinsic defects can be radiative ( $Cu^+/Cu^{2+}$ ) or nonradiative ( $In_{Cu}^{2+}$ ,  $V_{Cu}^{1-}$ ). Ligands dictate the preference of one path over another.

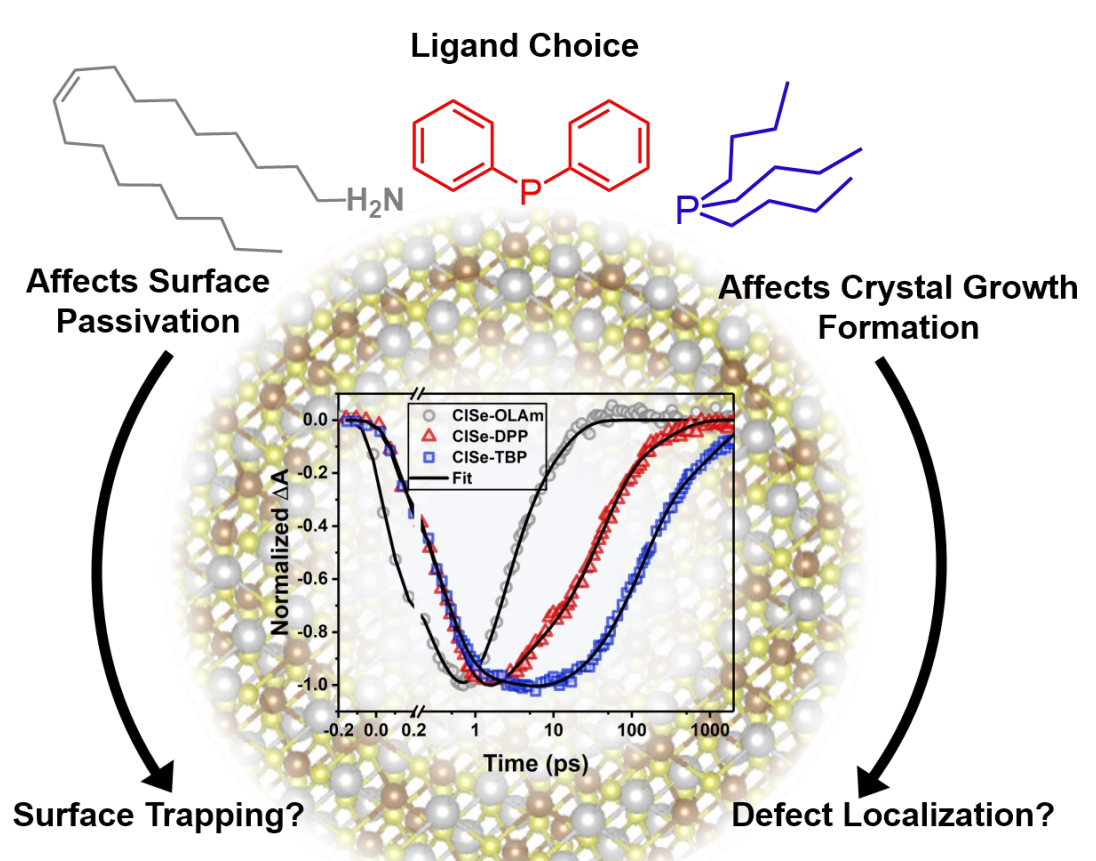
**Table 1:** Photophysical Properties and Device Efficiencies

	τ <sub>1</sub> (ps)	τ <sub>2</sub> (ps)	τ3 (ps)	τ4 (ps)	PLQY (%)	PV Device Efficiency
CISe- OLAm	$0.25 \pm 0.05$	0.42 ± 0.07	$1.9 \pm 0.2$	$9.3 \pm 0.7$	0.003	$0.5 \pm 0.3$
CISe-DPP	0.411 ± 0.009	$2.3 \pm 0.1$	39 ± 1	$250 \pm 14$	0.14	$0.84 \pm 0.09$
CISe-TBP	$0.336 \pm 0.008$	$3.4 \pm 0.2$	127 ± 2	$1110 \pm 30$	1.2	$1.5 \pm 0.3$

Table 2: Structural and Surface Characterizations

	Ratio of	Cu:In Ratio	Surface Coverage	% Phosphine				
	Raman Peaks		Ligands/nm <sup>2</sup>	Ligand				
CISe-OLAm	2.19	$0.936 \pm 0.006$	1.58	-				
CISe-DPP	1.78	$0.937 \pm 0.002$	1.76	18				
CISe-TBP	2.12	$0.806 \pm 0.008$	1.89	11				

# **TOC Graphic**



#### Radiative Recombination?

#### References

- 1. Panfil, Y. E.; Oded, M.; Banin, U., Colloidal Quantum Nanostructures: Emerging Materials for Display Applications. *Angew. Chem., Int. Ed.* **2018**, *57*, 4274-4295.
- 2. Choi, M. K.; Yang, J.; Hyeon, T.; Kim, D.-H., Flexible Quantum Dot Light-Emitting Diodes for Next-Generation Displays. *npj Flexible Electron.* **2018**, *2*, 10.
- 3. Erdem, T.; Demir, H. V., Color Science of Nanocrystal Quantum Dots for Lighting and Displays. *Nanophotonics* **2013**, *2*, 57-81.
- 4. Pietryga, J. M.; Park, Y.-S.; Lim, J.; Fidler, A. F.; Bae, W. K.; Brovelli, S.; Klimov, V. I., Spectroscopic and Device Aspects of Nanocrystal Quantum Dots. *Chem. Rev.* **2016**, *116*, 10513-10622.
- 5. Kamat, P. V., Quantum Dot Solar Cells. Semiconductor Nanocrystals as Light Harvesters. *J. Phys. Chem. C* **2008**, *112*, 18737-18753.
- 6. Hetsch, F.; Xu, X.; Wang, H.; Kershaw, S. V.; Rogach, A. L., Semiconductor Nanocrystal Quantum Dots as Solar Cell Components and Photosensitizers: Material, Charge Transfer, and Separation Aspects of Some Device Topologies. *J. Phys. Chem. Lett.* **2011**, *2*, 1879-1887.
- 7. Etgar, L., Semiconductor Nanocrystals as Light Harvesters in Solar Cells. *Materials* **2013**, *6*, 445-459.

- 8. Reiss, P., Synthesis of Semiconductor Nanocrystals in Organic Solvents. In *Semiconductor Nanocrystal Quantum Dots: Synthesis, Assembly, Spectroscopy and Applications*, Rogach, A. L., Ed. Springer Vienna: Vienna, 2008; pp 35-72.
- 9. Chang, J.; Waclawik, E. R., Colloidal Semiconductor Nanocrystals: Controlled Synthesis and Surface Chemistry in Organic Media. *RSC Adv.* **2014**, *4*, 23505-23527.
- 10. Kwon, S. G.; Hyeon, T., Colloidal Chemical Synthesis and Formation Kinetics of Uniformly Sized Nanocrystals of Metals, Oxides, and Chalcogenides. *Acc. Chem. Res.* **2008**, *41*, 1696-1709.
- 11. Evans, C. M.; Cass, L. C.; Knowles, K. E.; Tice, D. B.; Chang, R. P. H.; Weiss, E. A., Review of the Synthesis and Properties of Colloidal Quantum Dots: The Evolving Role of Coordinating Surface Ligands. *J. Coord. Chem.* **2012**, *65*, 2391-2414.
- 12. Harris, R. D.; Bettis Homan, S.; Kodaimati, M.; He, C.; Nepomnyashchii, A. B.; Swenson, N. K.; Lian, S.; Calzada, R.; Weiss, E. A., Electronic Processes within Quantum Dot-Molecule Complexes. *Chem. Rev.* **2016**, *116*, 12865-12919.
- 13. Zhou, J.; Liu, Y.; Tang, J.; Tang, W., Surface Ligands Engineering of Semiconductor Quantum Dots for Chemosensory and Biological Applications. *Mater. Today* **2017**, *20*, 360-376.
- 14. Hines, D. A.; Kamat, P. V., Quantum Dot Surface Chemistry: Ligand Effects and Electron Transfer Reactions. *J. Phys. Chem. C* **2013**, *117*, 14418-14426.
- 15. Peterson, M. D.; Cass, L. C.; Harris, R. D.; Edme, K.; Sung, K.; Weiss, E. A., The Role of Ligands in Determining the Exciton Relaxation Dynamics in Semiconductor Quantum Dots. *Annu. Rev. Phys. Chem.* **2014**, *65*, 317-339.
- 16. Nag, A.; Kovalenko, M. V.; Lee, J.-S.; Liu, W.; Spokoyny, B.; Talapin, D. V., Metalfree Inorganic Ligands for Colloidal Nanocrystals: S<sup>2-</sup>, HS<sup>-</sup>, Se<sup>2-</sup>, HSe<sup>-</sup>, Te<sup>2-</sup>, HTe<sup>-</sup>, TeS<sub>3</sub><sup>2-</sup>, OH<sup>-</sup>, and NH<sub>2</sub><sup>-</sup> as Surface Ligands. *J. Am. Chem. Soc.* **2011**, *133*, 10612-10620.
- 17. Giansante, C.; Infante, I., Surface Traps in Colloidal Quantum Dots: A Combined Experimental and Theoretical Perspective. *J. Phys. Chem. Lett.* **2017**, *8*, 5209-5215.
- 18. Harvey, S. M.; Houck, D. W.; Kirschner, M. S.; Flanders, N. C.; Brumberg, A.; Leonard, A. A.; Watkins, N. E.; Chen, L. X.; Dichtel, W. R.; Zhang, X.; Korgel, B. A.; Wasielewski, M. R.; Schaller, R. D., Transient Lattice Response upon Photoexcitation in CuInSe<sub>2</sub> Nanocrystals with Organic or Inorganic Surface Passivation. *ACS Nano* **2020**, *14*, 13548-13556.
- 19. Brown, P. R.; Kim, D.; Lunt, R. R.; Zhao, N.; Bawendi, M. G.; Grossman, J. C.; Bulović, V., Energy Level Modification in Lead Sulfide Quantum Dot Thin Films through Ligand Exchange. *ACS Nano* **2014**, *8*, 5863-5872.
- 20. Anderson, N. C.; Hendricks, M. P.; Choi, J. J.; Owen, J. S., Ligand Exchange and the Stoichiometry of Metal Chalcogenide Nanocrystals: Spectroscopic Observation of Facile Metal-Carboxylate Displacement and Binding. *J. Am. Chem. Soc.* **2013**, *135*, 18536-18548.
- 21. Houtepen, A. J.; Hens, Z.; Owen, J. S.; Infante, I., On the Origin of Surface Traps in Colloidal II–VI Semiconductor Nanocrystals. *Chem. Mater.* **2017**, *29*, 752-761.
- 22. Reiss, P.; Carrière, M.; Lincheneau, C.; Vaure, L.; Tamang, S., Synthesis of Semiconductor Nanocrystals, Focusing on Nontoxic and Earth-Abundant Materials. *Chem. Rev.* **2016**, *116*, 10731-10819.
- 23. Yarema, O.; Yarema, M.; Wood, V., Tuning the Composition of Multicomponent Semiconductor Nanocrystals: The Case of I–III–VI Materials. *Chem. Mater.* **2018**, *30*, 1446-1461.

- 24. Long, Z.; Zhang, W.; Tian, J.; Chen, G.; Liu, Y.; Liu, R., Recent Research on the Luminous Mechanism, Synthetic Strategies, and Applications of CuInS<sub>2</sub> Quantum Dots. *Inorg. Chem. Front.* **2021**, *8*, 880-897.
- 25. Aldakov, D.; Lefrançois, A.; Reiss, P., Ternary and Quaternary Metal Chalcogenide Nanocrystals: Synthesis, Properties and Applications. *J. Mater. Chem. C* **2013**, *1*, 3756-3776.
- 26. Zhang, S. B.; Wei, S.-H.; Zunger, A.; Katayama-Yoshida, H., Defect Physics of the CuInSe<sub>2</sub> Chalcopyrite Semiconductor. *Phys. Rev. B* **1998**, *57*, 9642-9656.
- 27. Rincón, C.; Márquez, R., Defect Physics of the CuInSe<sub>2</sub> Chalcopyrite Semiconductor. *J. Phys. Chem. Solids* **1999**, *60*, 1865-1873.
- 28. Jaffe, J. E.; Zunger, A., Defect-Induced Nonpolar-to-Polar Transition at the Surface of CuInSe<sub>2</sub>. *J. Phys. Chem. Solids* **2003**, *64*, 1547-1552.
- 29. Colombara, D.; Elanzeery, H.; Nicoara, N.; Sharma, D.; Claro, M.; Schwarz, T.; Koprek, A.; Wolter, M. H.; Melchiorre, M.; Sood, M.; Valle, N.; Bondarchuk, O.; Babbe, F.; Spindler, C.; Cojocaru-Miredin, O.; Raabe, D.; Dale, P. J.; Sadewasser, S.; Siebentritt, S., Chemical Instability at Chalcogenide Surfaces Impacts Chalcopyrite Devices Well Beyond the Surface. *Nat. Commun.* **2020**, *11*, 3634-3634.
- 30. Berends, A. C.; Mangnus, M. J. J.; Xia, C.; Rabouw, F. T.; de Mello Donega, C., Optoelectronic Properties of Ternary I–III–VI<sub>2</sub> Semiconductor Nanocrystals: Bright Prospects with Elusive Origins. *J. Phys. Chem. Lett.* **2019**, *10*, 1600-1616.
- 31. Leach, A. D. P.; Macdonald, J. E., Optoelectronic Properties of CuInS<sub>2</sub> Nanocrystals and Their Origin. *J. Phys. Chem. Lett.* **2016,** 7, 572-583.
- 32. Du, J.; Singh, R.; Fedin, I.; Fuhr, A. S.; Klimov, V. I., Spectroscopic Insights into High Defect Tolerance of Zn:CuInSe<sub>2</sub> Quantum-Dot-Sensitized Solar Cells. *Nat. Energy* **2020**, *5*, 409-417.
- 33. Madelung, O., I-III-VI<sub>2</sub> Compounds. In *Semiconductors: Data Handbook*, Madelung, O., Ed. Springer Berlin Heidelberg: Berlin, Heidelberg, 2004; pp 289-328.
- 34. Madelung, O., Elements of the IVth group and IV-IV Compounds. In *Semiconductors: Data Handbook*, Madelung, O., Ed. Springer Berlin Heidelberg: Berlin, Heidelberg, 2004; pp 7-70.
- 35. Kang, X.; Yang, Y.; Huang, L.; Tao, Y.; Wang, L.; Pan, D., Large-Scale Synthesis of Water-Soluble CuInSe<sub>2</sub>/ZnS and AgInSe<sub>2</sub>/ZnS Core/Shell Quantum Dots. *Green Chem.* **2015**, *17*, 4482-4488.
- 36. Lu, H.; Carroll, G. M.; Neale, N. R.; Beard, M. C., Infrared Quantum Dots: Progress, Challenges, and Opportunities. *ACS Nano* **2019**, *13*, 939-953.
- 37. Haloui, H.; Touafek, K.; Zaabat, M.; hocine, H. B. c. e.; Khelifa, A., The Copper Indium Selenium (CuInSe<sub>2</sub>) Thin Films Solar Cells for Hybrid Photovoltaic Thermal Collectors (PVT). *Energy Procedia* **2015**, *74*, 1213-1219.
- 38. Feurer, T.; Carron, R.; Torres Sevilla, G.; Fu, F.; Pisoni, S.; Romanyuk, Y. E.; Buecheler, S.; Tiwari, A. N., Efficiency Improvement of Near-Stoichiometric CuInSe<sub>2</sub> Solar Cells for Application in Tandem Devices. *Adv. Energy Mater.* **2019**, *9*, 1901428.
- 39. Liu, F.; Zeng, Q.; Li, J.; Hao, X.; Ho-Baillie, A.; Tang, J.; Green, M. A., Emerging Inorganic Compound Thin Film Photovoltaic Materials: Progress, Challenges and Strategies. *Mater. Today* **2020**, *41*, 120-142.
- 40. Feurer, T.; Reinhard, P.; Avancini, E.; Bissig, B.; Löckinger, J.; Fuchs, P.; Carron, R.; Weiss, T. P.; Perrenoud, J.; Stutterheim, S.; Buecheler, S.; Tiwari, A. N., Progress in Thin Film

- CIGS photovoltaics Research and Development, Manufacturing, and Applications. *Prog. Photovoltaics* **2017**, *25*, 645-667.
- 41. Kato, T., Cu(In,Ga)(Se,S)<sub>2</sub> Solar Cell Research in Solar Frontier: Progress and Current Status. *Jpn. J. Appl. Phys.* **2017**, *56*, 04CA02.
- 42. Voggu, V. R.; Sham, J.; Pfeffer, S.; Pate, J.; Fillip, L.; Harvey, T. B.; Brown, R. M.; Korgel, B. A., Flexible CuInSe<sub>2</sub> Nanocrystal Solar Cells on Paper. *ACS Energy Lett.* **2017**, *2*, 574-581.
- 43. Akhavan, V. A.; Goodfellow, B. W.; Panthani, M. G.; Reid, D. K.; Hellebusch, D. J.; Adachi, T.; Korgel, B. A., Spray-Deposited CuInSe<sub>2</sub> Nanocrystal Photovoltaics. *Energy Environ. Sci.* **2010**, *3*, 1600-1606.
- 44. Stolle, C. J.; Harvey, T. B.; Korgel, B. A. Photonic Curing of Ligand-Capped CuInSe<sub>2</sub> Nanocrystal Films. In Proceedings of the 2014 IEEE 40th Photovoltaic Specialist Conference (PVSC); Denver, June 8–13, 2004; IEEE: Piscataway, NJ, 2014; pp 0270–0274
- 45. Stolle, C. J.; Panthani, M. G.; Harvey, T. B.; Akhavan, V. A.; Korgel, B. A., Comparison of the Photovoltaic Response of Oleylamine and Inorganic Ligand-Capped CuInSe<sub>2</sub> Nanocrystals. *ACS Appl. Mater. Interfaces* **2012**, *4*, 2757-2761.
- 46. Guo, J.; Wang, X.; Zhou, W.-H.; Chang, Z.-X.; Wang, X.; Zhou, Z.-J.; Wu, S.-X., Efficiency Enhancement of Dye-Sensitized Solar Cells (DSSCs) Using Ligand Exchanged CuInS<sub>2</sub> NCs as Counter Electrode Materials. *RSC Adv.* **2013**, *3*, 14731-14736.
- 47. Zheng, Y.; Sadeghimakki, B.; Brunning, J. A. L.; Sivoththaman, S., Ligand Exchange Functionalization of CIS Quantum Dots for CIS/ZnO Film Heterojunctions. *IEEE Trans. Nanotechnol.* **2019**, *18*, 728-733.
- 48. Reinhold, H.; Mikolajczak, U.; Brand, I.; Dosche, C.; Borchert, H.; Parisi, J.; Scheunemann, D., Shorter Is Not Always Better: Analysis of a Ligand Exchange Procedure for CuInS<sub>2</sub> Nanoparticles as the Photovoltaic Absorber Material. *J. Phys. Chem. C* **2020**, *124*, 19922-19928.
- 49. Bujak, P., Core and Surface Engineering in Binary, Ternary and Quaternary Semiconductor Nanocrystals—A Critical Review. *Synth. Met.* **2016**, *222*, 93-114.
- 50. Tappan, B. A.; Barim, G.; Kwok, J. C.; Brutchey, R. L., Utilizing Diselenide Precursors toward Rationally Controlled Synthesis of Metastable CuInSe<sub>2</sub> Nanocrystals. *Chem. Mater.* **2018**, *30*, 5704-5713.
- 51. Stolle, C. J.; Schaller, R. D.; Korgel, B. A., Efficient Carrier Multiplication in Colloidal CuInSe<sub>2</sub> Nanocrystals. *J. Phys. Chem. Lett.* **2014**, *5*, 3169-3174.
- 52. Houck, D. W.; Korgel, B. A., Facile Exchange of Tightly Bonded L-Type Oleylamine and Diphenylphosphine Ligands on Copper Indium Diselenide Nanocrystals Mediated by Molecular Iodine. *Chem. Mater.* **2018**, *30*, 8359-8367.
- 53. Panthani, M. G.; Akhavan, V.; Goodfellow, B.; Schmidtke, J. P.; Dunn, L.; Dodabalapur, A.; Barbara, P. F.; Korgel, B. A., Synthesis of CuInS<sub>2</sub>, CuInSe<sub>2</sub>, and Cu(In<sub>x</sub>Ga<sub>1-x</sub>)Se<sub>2</sub> (CIGS) Nanocrystal "Inks" for Printable Photovoltaics. *J. Am. Chem. Soc.* **2008**, *130*, 16770-16777.
- 54. Akhavan, V. A.; Panthani, M. G.; Goodfellow, B. W.; Reid, D. K.; Korgel, B. A., Thickness-Limited Performance of CuInSe<sub>2</sub> Nanocrystal Photovoltaic Devices. *Opt. Express* **2010**, *18*, A411-A420.
- 55. Zanatta, A. R., Revisiting the Optical Bandgap of Semiconductors and the Proposal of a Unified Methodology to its Determination. *Sci. Rep.* **2019**, *9*, 11225.

- 56. Klimov, V. I., Optical Nonlinearities and Ultrafast Carrier Dynamics in Semiconductor Nanocrystals. *J. Phys. Chem. B* **2000**, *104*, 6112-6123.
- 57. Klimov, V. I.; Schwarz, C. J.; McBranch, D. W.; Leatherdale, C. A.; Bawendi, M. G., Ultrafast Dynamics of Inter- and Intraband Transitions in Semiconductor Nanocrystals: Implications for Quantum-Dot Lasers. *Phys. Rev. B* **1999**, *60*, R2177-R2180.
- 58. Kraatz, I. T.; Booth, M.; Whitaker, B. J.; Nix, M. G. D.; Critchley, K., Sub-Bandgap Emission and Intraband Defect-Related Excited-State Dynamics in Colloidal CuInS<sub>2</sub>/ZnS Quantum Dots Revealed by Femtosecond Pump–Dump–Probe Spectroscopy. *J. Phys. Chem. C* **2014**, *118*, 24102-24109.
- 59. Sun, J.; Zhu, D.; Zhao, J.; Ikezawa, M.; Wang, X.; Masumoto, Y., Ultrafast Carrier Dynamics in CuInS<sub>2</sub> Quantum Dots. *Appl. Phys. Lett.* **2014**, *104*, 023118.
- 60. Debnath, T.; Ghosh, H. N., Ternary Metal Chalcogenides: Into the Exciton and Biexciton Dynamics. *J. Phys. Chem. Lett.* **2019**, *10*, 6227-6238.
- 61. Klimov, V. I., Spectral and Dynamical Properties of Multiexcitons in Semiconductor Nanocrystals. *Annu. Rev. Phys. Chem.* **2007**, *58*, 635-673.
- 62. Guyot-Sionnest, P.; Hines, M. A., Intraband Transitions in Semiconductor Nanocrystals. *Appl. Phys. Lett.* **1998**, *72*, 686-688.
- 63. Chang, A. Y.; Liu, W.; Talapin, D. V.; Schaller, R. D., Carrier Dynamics in Highly Quantum-Confined, Colloidal Indium Antimonide Nanocrystals. *ACS Nano* **2014**, *8*, 8513-8519.
- 64. Houck, D. W.; Assaf, E. I.; Shin, H.; Greene, R. M.; Pernik, D. R.; Korgel, B. A., Pervasive Cation Vacancies and Antisite Defects in Copper Indium Diselenide (CuInSe<sub>2</sub>) Nanocrystals. *J. Phys. Chem. C* **2019**, *123*, 9544-9551.
- 65. Reena Philip, R.; Pradeep, B., Nonideal Anion Displacement, Band Gap Variation, and Valence Band Splitting in Cu–In–Se Compounds. *Thin Solid Films* **2005**, *472*, 136-143.
- 66. Rincón, C.; Ramírez, F. J., Lattice Vibrations of CuInSe<sub>2</sub> and CuGaSe<sub>2</sub> by Raman Microspectrometry. *J. Appl. Phys.* **1992**, *72*, 4321-4324.
- 67. Goldzak, T.; McIsaac, A. R.; Van Voorhis, T., Colloidal CdSe Nanocrystals are Inherently Defective. *Nat. Commun.* **2021**, *12*, 890.
- 68. Jasieniak, J.; Mulvaney, P., From Cd-Rich to Se-Rich the Manipulation of CdSe Nanocrystal Surface Stoichiometry. *J. Am. Chem. Soc.* **2007**, *129*, 2841-2848.
- 69. Gadzhiev, T. M.; Babaev, A. A.; Gadzhieva, R. M.; Magomedova, D. K.; Khokhlachev, P. P., Properties of CuInSe<sub>2</sub> Films Obtained by Methods of Selenization and Quasi-Equilibrium Deposition. *Inorg. Mater.* **2008**, *44*, 1295.
- 70. Yarema, O.; Bozyigit, D.; Rousseau, I.; Nowack, L.; Yarema, M.; Heiss, W.; Wood, V., Highly Luminescent, Size- and Shape-Tunable Copper Indium Selenide Based Colloidal Nanocrystals. *Chem. Mater.* **2013**, *25*, 3753-3757.
- 71. Zhong, H.; Wang, Z.; Bovero, E.; Lu, Z.; van Veggel, F. C. J. M.; Scholes, G. D., Colloidal CuInSe<sub>2</sub> Nanocrystals in the Quantum Confinement Regime: Synthesis, Optical Properties, and Electroluminescence. *J. Phys. Chem. C* **2011**, *115*, 12396-12402.
- 72. Fuhr, A. S.; Yun, H. J.; Makarov, N. S.; Li, H.; McDaniel, H.; Klimov, V. I., Light Emission Mechanisms in CuInS<sub>2</sub> Quantum Dots Evaluated by Spectral Electrochemistry. *ACS Photonics* **2017**, *4*, 2425-2435.
- 73. van der Stam, W.; de Graaf, M.; Gudjonsdottir, S.; Geuchies, J. J.; Dijkema, J. J.; Kirkwood, N.; Evers, W. H.; Longo, A.; Houtepen, A. J., Tuning and Probing the Distribution of Cu<sup>+</sup> and Cu<sup>2+</sup> Trap States Responsible for Broad-Band Photoluminescence in CuInS<sub>2</sub> Nanocrystals. *ACS Nano* **2018**, *12*, 11244-11253.

- 74. Knowles, K. E.; Nelson, H. D.; Kilburn, T. B.; Gamelin, D. R., Singlet–Triplet Splittings in the Luminescent Excited States of Colloidal Cu<sup>+</sup>:CdSe, Cu<sup>+</sup>:InP, and CuInS<sub>2</sub> Nanocrystals: Charge-Transfer Configurations and Self-Trapped Excitons. *J. Am. Chem. Soc.* **2015**, *137*, 13138-13147.
- 75. Rice, W. D.; McDaniel, H.; Klimov, V. I.; Crooker, S. A., Magneto-Optical Properties of CuInS<sub>2</sub> Nanocrystals. *J. Phys. Chem. Lett.* **2014**, *5*, 4105-4109.
- 76. Rowland, C. E.; Fedin, I.; Diroll, B. T.; Liu, Y.; Talapin, D. V.; Schaller, R. D., Elevated Temperature Photophysical Properties and Morphological Stability of CdSe and CdSe/CdS Nanoplatelets. *J. Phys. Chem. Lett.* **2018**, *9*, 286-293.
- 77. Rowland, C. E.; Schaller, R. D., Exciton Fate in Semiconductor Nanocrystals at Elevated Temperatures: Hole Trapping Outcompetes Exciton Deactivation. *J. Phys. Chem. C* **2013**, *117*, 17337-17343.
- 78. Rowland, C. E.; Hannah, D. C.; Demortière, A.; Yang, J.; Cook, R. E.; Prakapenka, V. B.; Kortshagen, U.; Schaller, R. D., Silicon Nanocrystals at Elevated Temperatures: Retention of Photoluminescence and Diamond Silicon to β-Silicon Carbide Phase Transition. *ACS Nano* **2014**, *8*, 9219-9223.
- 79. Rowland, C. E.; Liu, W.; Hannah, D. C.; Chan, M. K. Y.; Talapin, D. V.; Schaller, R. D., Thermal Stability of Colloidal InP Nanocrystals: Small Inorganic Ligands Boost High-Temperature Photoluminescence. *ACS Nano* **2014**, *8*, 977-985.
- 80. Saniz, R.; Bekaert, J.; Partoens, B.; Lamoen, D., Structural and Electronic Properties of Defects at Grain Boundaries in CuInSe<sub>2</sub>. *Phys. Chem. Chem. Phys.* **2017**, *19*, 14770-14780.
- 81. Xie, B.-B.; Hu, B.-B.; Jiang, L.-F.; Li, G.; Du, Z.-L., The Phase Transformation of CuInS<sub>2</sub> from Chalcopyrite to Wurtzite. *Nanoscale Res. Lett.* **2015**, *10*, 86.
- 82. Behera, P. S.; Rajesh, D.; Karthikeyan, S.; Sunandana, C. S.; Mohan, D. B., Study of Quasi-Amorphous to Nanocrystalline Phase Transition in Thermally Evaporated CuInS<sub>2</sub> Thin Films. *J. Mater. Res.* **2014**, *29*, 542-555.
- 83. Li, S.; Zhao, Z.; Liu, Q.; Huang, L.; Wang, G.; Pan, D.; Zhang, H.; He, X., Alloyed (ZnSe)<sub>x</sub>(CuInSe<sub>2</sub>)<sub>1-x</sub> and CuInSe<sub>x</sub>S<sub>2-x</sub> Nanocrystals with a Monophase Zinc Blende Structure over the Entire Composition Range. *Inorg. Chem.* **2011**, *50*, 11958-11964.
- 84. Hens, Z.; Martins, J. C., A Solution NMR Toolbox for Characterizing the Surface Chemistry of Colloidal Nanocrystals. *Chem. Mater.* **2013**, *25*, 1211-1221.
- 85. García-Rodríguez, R.; Hendricks, M. P.; Cossairt, B. M.; Liu, H.; Owen, J. S., Conversion Reactions of Cadmium Chalcogenide Nanocrystal Precursors. *Chem. Mater.* **2013**, *25*, 1233-1249.
- 86. Dierick, R.; Van den Broeck, F.; De Nolf, K.; Zhao, Q.; Vantomme, A.; Martins, J. C.; Hens, Z., Surface Chemistry of CuInS<sub>2</sub> Colloidal Nanocrystals, Tight Binding of L-Type Ligands. *Chem. Mater.* **2014**, *26*, 5950-5957.
- 87. Henderson, W. A.; Streuli, C. A., The Basicity of Phosphines. *J. Am. Chem. Soc.* **1960**, 82, 5791-5794.
- 88. Castro, S. L.; Bailey, S. G.; Raffaelle, R. P.; Banger, K. K.; Hepp, A. F., Synthesis and Characterization of Colloidal CuInS<sub>2</sub> Nanoparticles from a Molecular Single-Source Precursor. *J. Phys. Chem. B* **2004**, *108*, 12429-12435.
- 89. Kovalenko, M. V.; Scheele, M.; Talapin, D. V., Colloidal Nanocrystals with Molecular Metal Chalcogenide Surface Ligands. *Science* **2009**, *324*, 1417.
- 90. Owen, J., The Coordination Chemistry of Nanocrystal Surfaces. *Science* **2015**, *347*, 615.

- 91. Moodelly, D.; Kowalik, P.; Bujak, P.; Pron, A.; Reiss, P., Synthesis, Photophysical Properties and Surface Chemistry of Chalcopyrite-Type Semiconductor Nanocrystals. *J. Mater. Chem. C* **2019**, *7*, 11665-11709.
- 92. Pinchetti, V.; Lorenzon, M.; McDaniel, H.; Lorenzi, R.; Meinardi, F.; Klimov, V. I.; Brovelli, S., Spectro-Electrochemical Probing of Intrinsic and Extrinsic Processes in Exciton Recombination in I–III–VI<sub>2</sub> Nanocrystals. *Nano Lett.* **2017**, *17*, 4508-4517.
- 93 Semonin, O. E.; Johnson, J. C.; Luther, J. M.; Midgett, A. G.; Nozik, A. J.; Beard, M. C., Absolute Photoluminescence Quantum Yields of IR-26 Dye, PbS, and PbSe Quantum Dots. *J. Phys. Chem. Lett.* **2010**, *1*, 2445-2450.
- Panthani, M. G.; Stolle, C. J.; Reid, D. K.; Rhee, D. J.; Harvey, T. B.; Akhavan, V. A.; Yu, Y.; Korgel, B. A., CuInSe<sub>2</sub> Quantum Dot Solar Cells with High Open-Circuit Voltage. *J. Phys. Chem. Lett.* **2013**, *4*, 2030-2034.
- Akhavan, V. A.; CuInSe<sub>2</sub> Quantum Dot Solar Cells, M. G.; Goodfellow, B. W.; Reid, D. K.; Korgel, B. A., Thickness-limited performance of CuInSe<sub>2</sub> nanocrystal photovoltaic devices. *Opt. Express* **2010**, *18*, A411-A420.
- McCandless, B. E.; Shafarman, W. N. Chemical Surface Deposition of Ultra-Thin Semiconductors. U.S. Patent 6537845B1 August 30, 2001.